Supporting Information

$MgSO_4$ as an Effective, Low Temperature Sulfur Dopant for Carbon Materials Enabling Fast Sodium Storage

*Sara Payá[a], Noel Díez[a], Jon Cottom[b,c], Emilia Olsson[b,c], Marta Sevilla[*a]*

[a]Instituto de Ciencia y Tecnología del Carbono (INCAR), CSIC
Francisco Pintado Fe 26, 33011 Oviedo, Spain
[b] *Advanced Research Center for Nanolithography, Science Park 106, Amsterdam, 1098 XG, The Netherlands*
[c]*Institute of Theoretical Physics, Institute of Physics, University of Amsterdam, Science Park 904, Amsterdam, 1098 XH, The Netherlands*

* Corresponding author: martasev@incar.csic.es

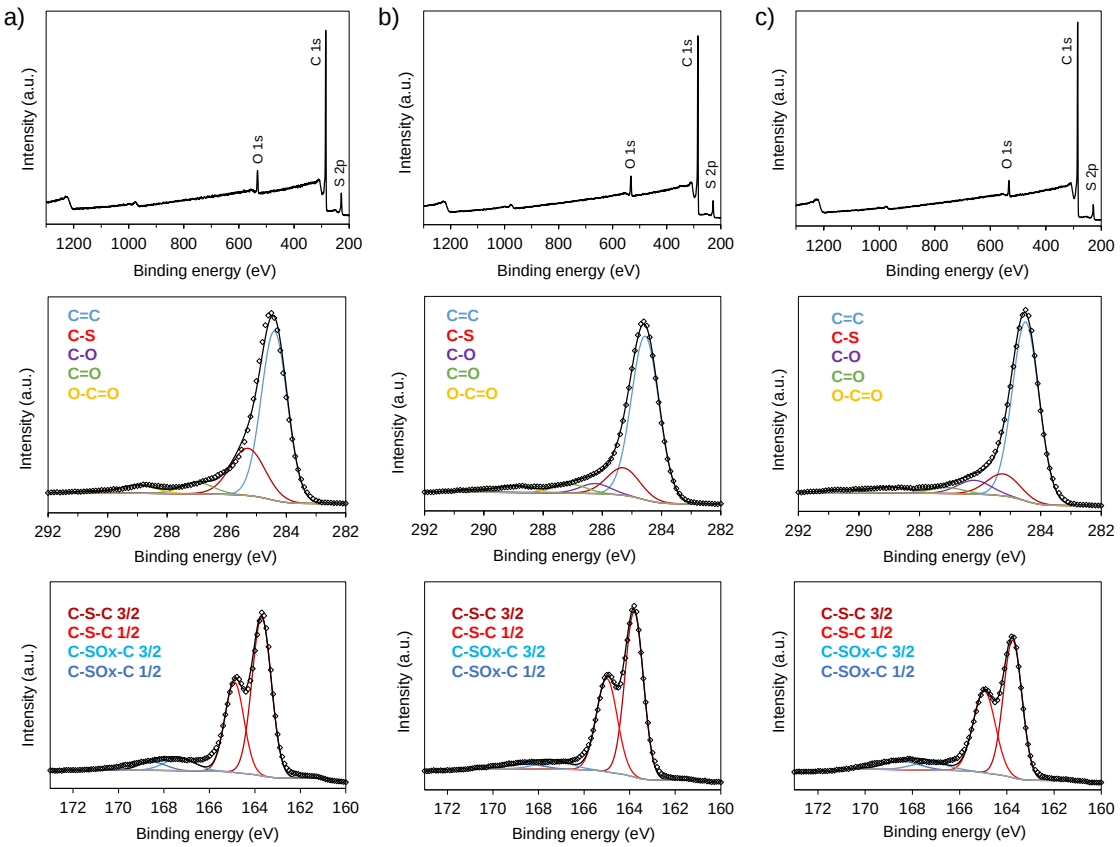

Figure S1. XPS general and high-resolution C 1s and S 2p spectra corresponding to a) G-Mg-600, b) G-Mgt-600 and c) G-Mgt-700. The decrease in S content with the increase of the carbonization/doping temperature observed by elemental analysis was confirmed by the quantification based on the general spectra (9.2 at% for G-Mgt-600 and 7.7 at% for G-Mgt-700), as well as by the decrease in the C-S signal identified in the C 1s high resolution spectra. The S 2p high resolution spectra was deconvoluted into two doublets at 165.1/163.9 eV, corresponding to C-S bonds, and 1.67.4/168.6 eV, which correspond to oxidized sulfur species (C-SO_x-S). No significant changes in S speciation were observed neither with the use of template nor with the increase of the temperature.

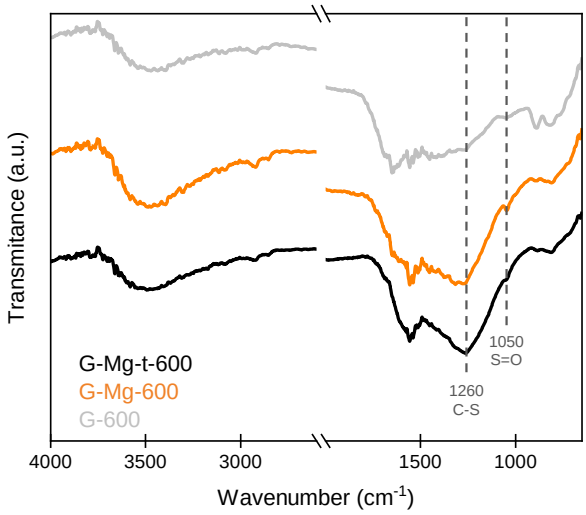

Figure S2. FTIR spectra of G-600, G-Mg-600 and G-Mg-t-600.

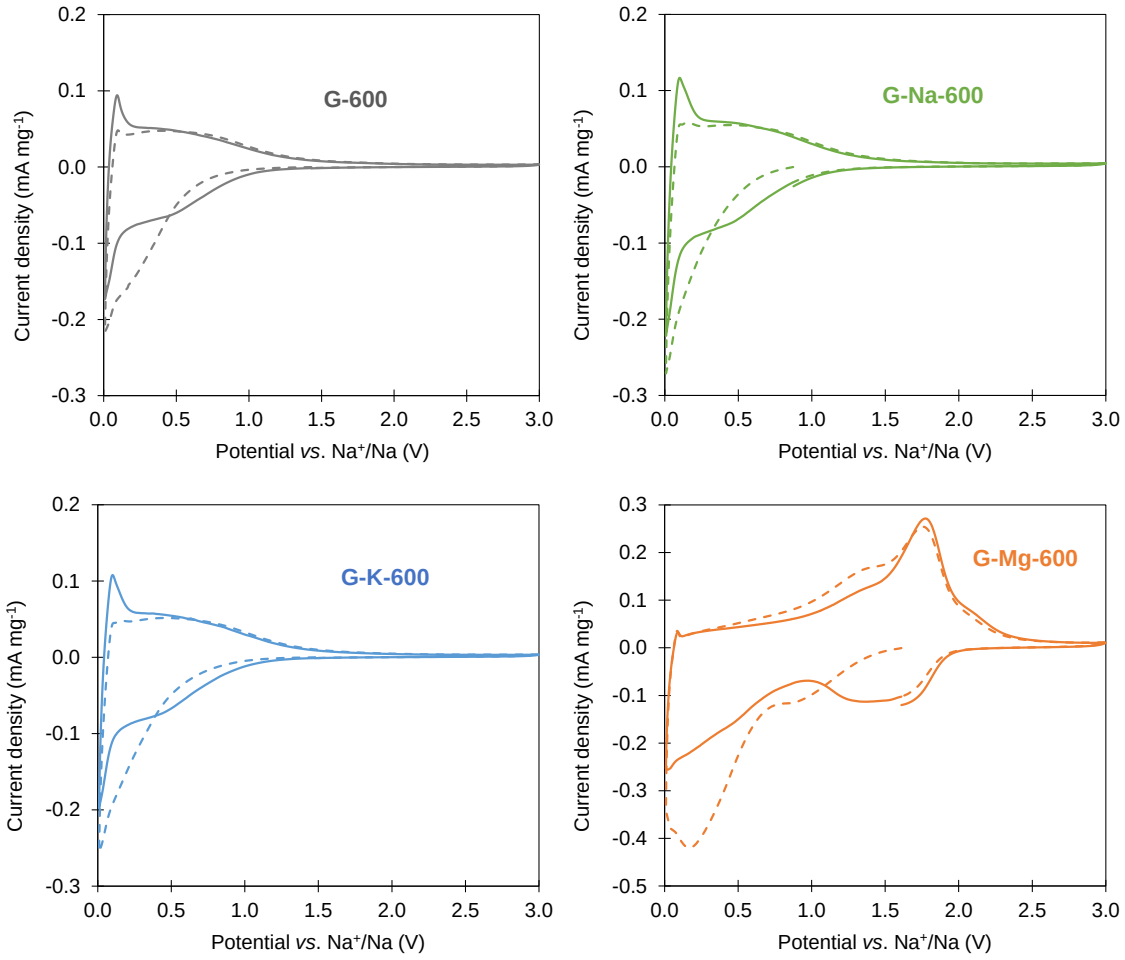

Figure S3. CVs recorded at 0.1 mV s^{-1} corresponding to the first (dashed line) and second cycle for the materials synthesized with different sulfates and without any sulfate.

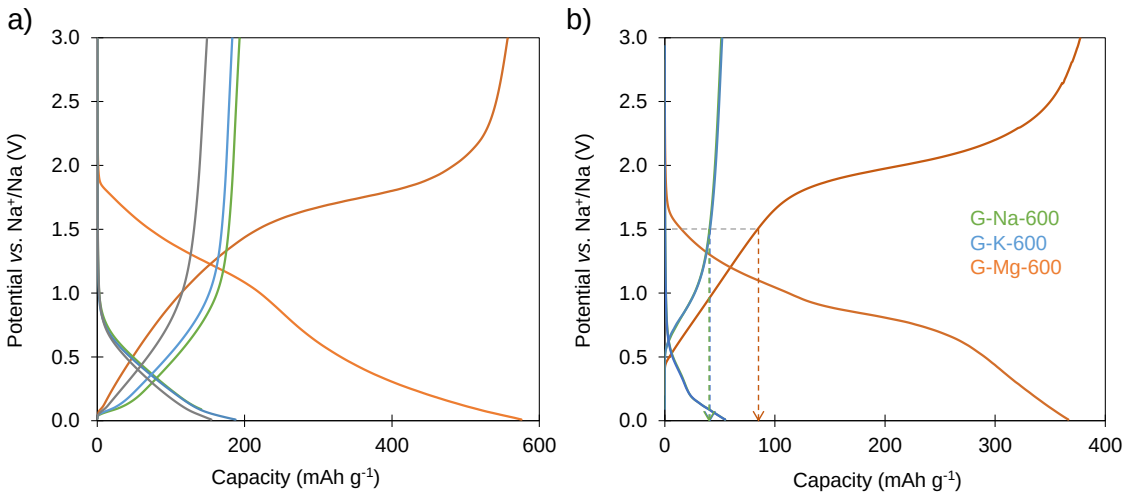

Figure S4. a) GCD profiles of materials corresponding to the second cycle at a) 0.1 A g^{-1} and b) 2 A g^{-1}.

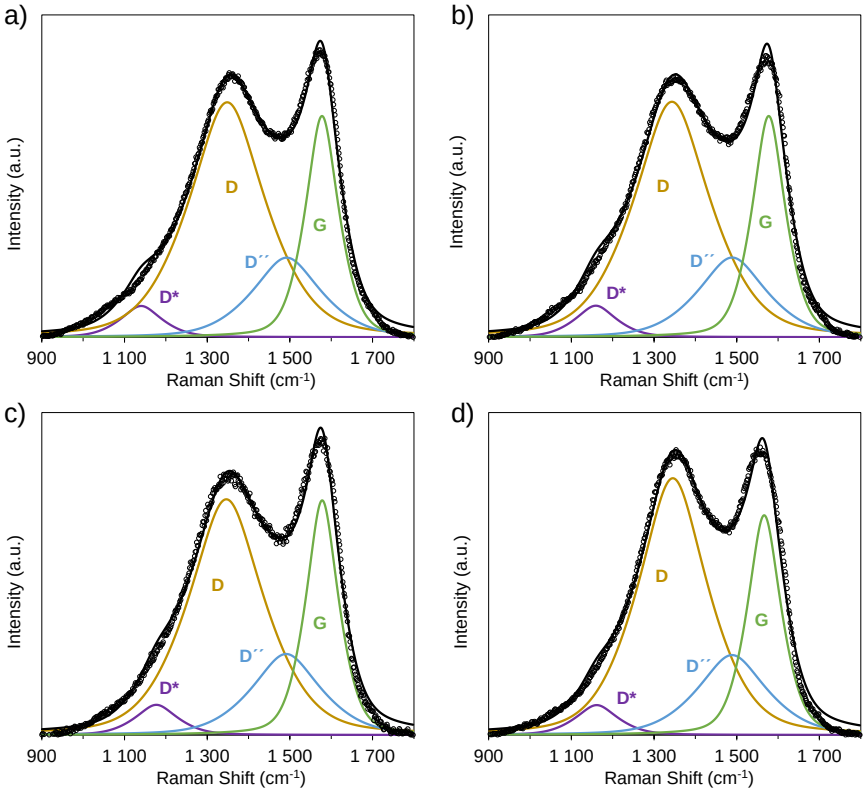

Figure S5. Deconvolution of the Raman spectra of a) G-Mg-600, b) G-Mg-t-600, c) TA-Mg-t-600 and d) PS-Mg-t-600.

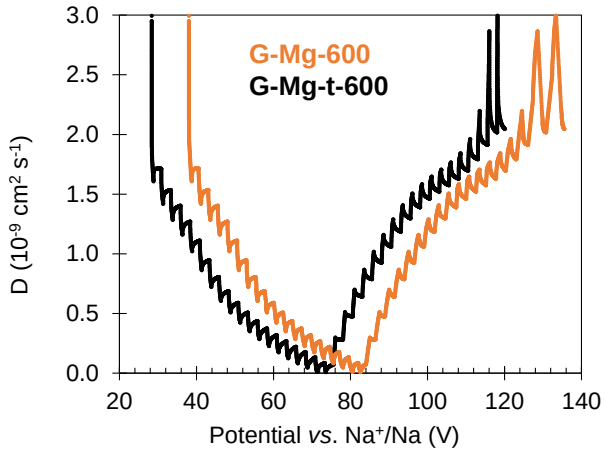

Figure S6. GITT potential profiles of samples synthesized with and without template.

Supplementary Note 1: The course of the carbonization process for the G-Mg-t-600 sample was monitored by analysing the crystallography of the products obtained at different temperatures and by the TGA-MS analysis of the starting mixture. As can be seen in **Figure S7a**, magnesium sulfate, together with sodium chloride, is still present at a temperature of 500 ºC. Above this temperature, the sulfate oxidizes the carbon material, doping it simultaneously with covalent sulfur, yielding MgO as a solid reaction product. At 600 ºC, together with MgO, the formation of a crystal phase with two diffraction peaks at 2θ = 23-24º is also observed (zoom in **Figure S7a**). This compound likely results from the chemical interaction between NaCl and $MgSO_4$ at *ca*. 600 ºC. Indeed, when the carbonization was conducted in the absence of NaCl, this intermediate substance was not identified and, instead, some unreacted $MgSO_4$ still remained in the carbonization product (**Figure 1a**). These observations can explain the lower degree of doping achieved by the samples prepared in the presence of NaCl. At 650 ºC, conversion of $MgSO_4$ to MgO is completed, and only the oxide and NaCl remain as impurities in the carbonized product. Analysis of TGA-MS curves show that the redox reactions between carbon and $MgSO_4$

are displaced towards higher temperatures in the presence of NaCl (**Figure S7b**) likely due to the formation of this intermediate product.

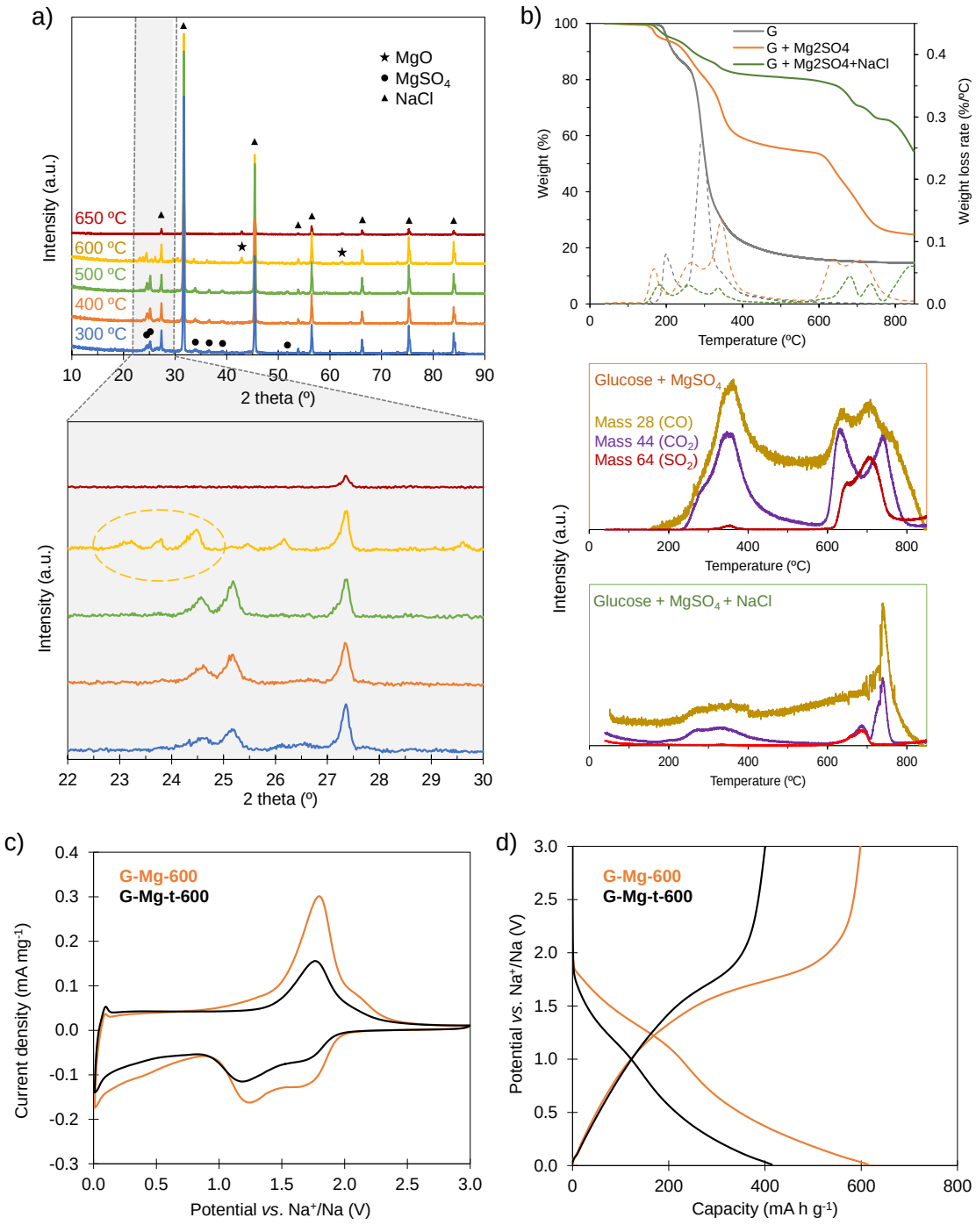

Figure S7. a) X-ray diffractograms of unpurified S-doped materials synthesized at different temperatures with zoom in the range of 2θ = 22-30º, b) TGA-MS analysis, c)

CVs recorded at a potential sweep rate of 0.1 mV s^{-1} for the samples with and without template, d) galvanostatic plots obtained at 0.1 A g^{-1} corresponding to the second cycle within the range 0.01-3 V *vs.* Na^+/Na.

Supplementary note 2: All DFT calculations were performed at the gamma point using CP2K, with GTH-pseudopotentials employed to describe the core electrons and DZVP-SR-MOLOPT basis sets utilized for the valence electrons. [1–7] The Perdew-Burke-Ernzerhof (PBE) functional was used in conjunction with the D3(BJ) dispersion correction to account for van der Waals interactions. [8–13] A convergence criterion of 0.1 meV was achieved with an energy cutoff of 650 Ry and a relative cutoff of 60 Ry. The lattice vectors of the orthogonal reconstruction of the 96-384 atom cells were relaxed for the defect-free system, and this optimized structure served as the basis for all subsequent calculations.

S-Doping was explored in the 1–30% range by symmetric enumeration of sulfur-substituted carbon (S_C) in graphene to approximate the basal plane of hard carbon following on the methodology of our previous studies. [14–21] Three initial configurations were considered: the pristine defect-free system, the carbon vacancy system, and the Stone-Wales defect. This resulted in 2632 configurations, for which the geometries were relaxed, and the formation energies extracted. The formation energies were calculated using the following relationship:

$$E_{form} = \frac{E_d - \left(E_{ref} + n_S\mu_S - n_C\mu_C\right)}{n_S}$$

where E_d is the total energy of the doped system, E_{ref} is the total energy of the reference (undoped) system, n_x are the number of C / S atom<s, and μ_x is the chemical potential, where x is sulphur or carbon. The chemical potentials for the S and C are taken from the elemental references.

The geometries of the systems were characterized based on the S-C and S-S bond lengths, with mean values per cell and their distributions reported for accessibility. Additionally, the roughness or rumpling of the carbon sheet was determined by calculating the standard deviation of the z-component of each atomic site relative to the undoped reference. The ring systems associated with the S-dopants were characterized using a graph representation, employing the NetworkX library to identify rings within the system. Rings containing sulphur atoms were screened, and the number of 5-membered and 6-membered sulphur-containing rings was compared. In addition, a Mulliken charge analysis was performed for all the systems.

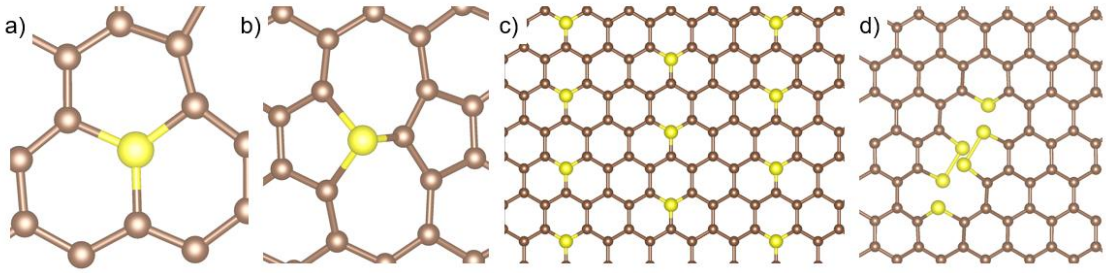

Figure S8. Models showing examples of a) the S-substitutional defect on a C site in the C_6 unit, b) S substitution in a Stone Wales defect, c) tessellation of 6-coordinated S-dopants and d) S defects leading to edge dislocation. Brown spheres represent C, and yellow S.

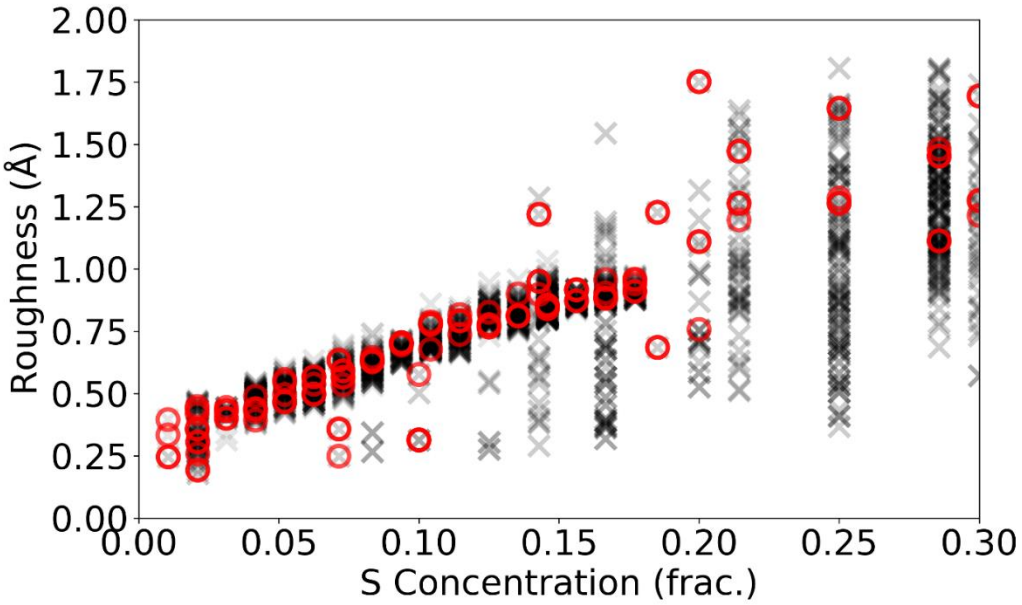

Figure S9. Sheet roughness as a function of sulphur concentration. Red circles denote the lowest energy configurations identified in Figure 6 in the main manuscript. Between 0 and 18 % S there is a gradual increase in the roughness as the rumpling of the sheet increases. Above 18 % the smooth trend gives way to a much greater variation in values; this variation is driven by the onset of S-cluster formation and increased propensity for S-capped linear dislocations to form. Geometrically, at low concentrations, S occupies the C-site with significant distortion, puckering out of the surface. In the pristine system, these orderings dominate in the 1–12% [S] range with very similar geometries and formation energies. Above 12%, S-capped dislocations to the lattice become increasingly favoured and dominate the low-energy structures above 14% [S]. The same trends are present in the defective systems; however, the S-capped dislocations become favourable above 5% [S]. In both cases, the capping-S is incorporated in a 5-membered ring.

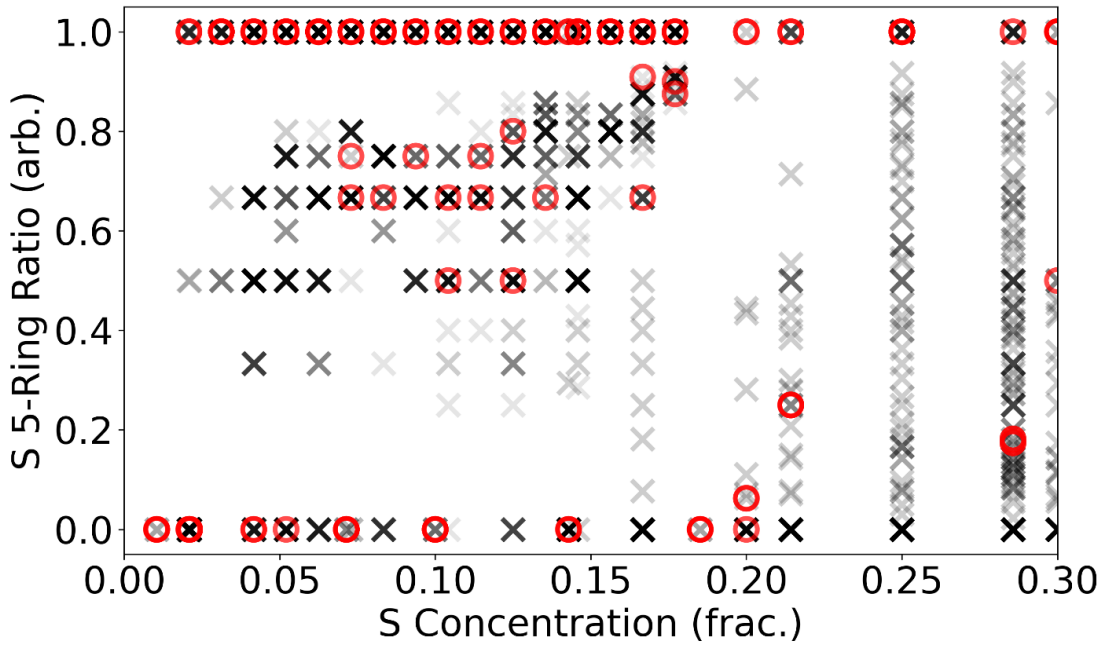

Figure S10. Five-membered sulphur rings in carbon sheet as a function of sulphur concentration. These observations provide atomic-scale insights into S-incorporation environment that places S in a 5-membered ring. Red circles denote the lowest energy configurations identified in Figure 6 in the main manuscript.

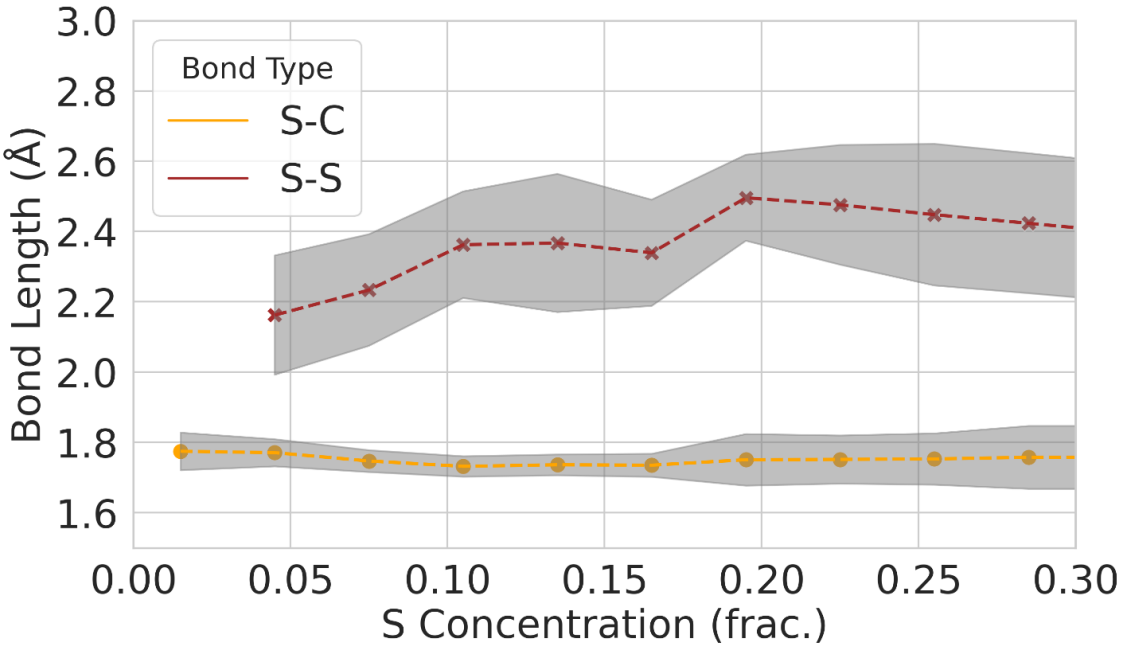

Figure S11. Bond length change as a function of sulphur concentration. The grey shaded area shows the spread of bond lengths. Consideration of the bond length shows the C-S remains in a narrow range centered on 1.77 Å at all [S] with a small increase above 18% [S]. In terms of the S-S distance, there is a small increase to ~2.4 Å. Above 20% [S], there is an increasing propensity to form S-S clusters, which drives the greater range of S-C and S-S bond lengths observed.

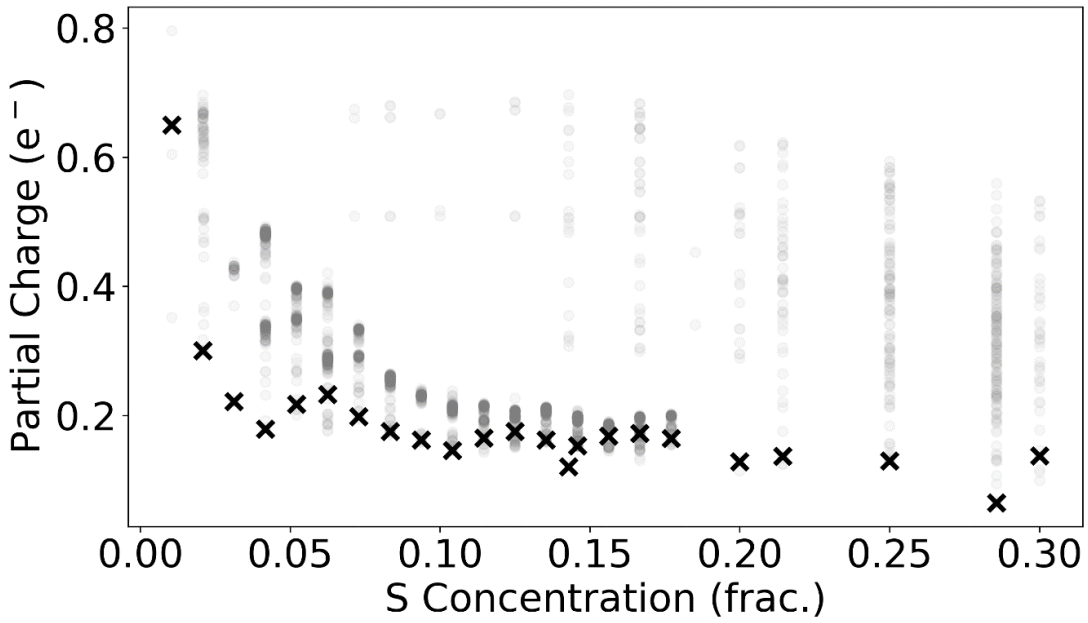

Figure S12. Mulliken charge as a function of sulphur concentration, showing that there is a charge transfer from S to C. At low concentrations, this is extremely pronounced, reducing as [S] increases, driven by the geometric distortions at higher [S] resulting in the S being more readily incorporated into the network. The crosses represent the energy weighted average charge.

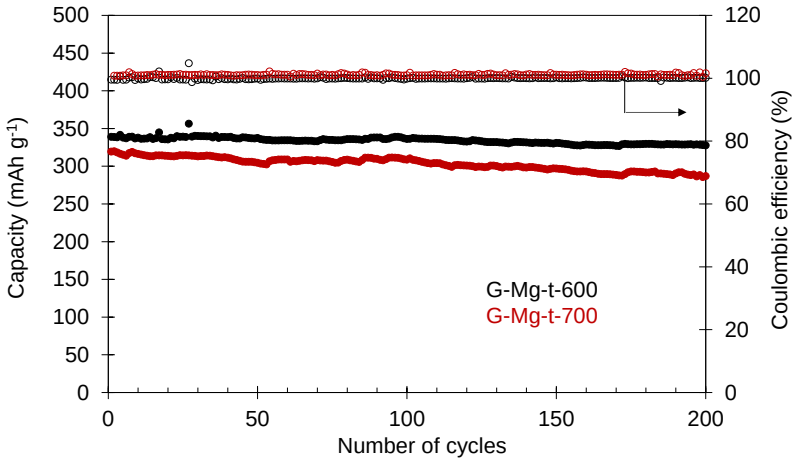

Figure S13. Long-term cycling stability at 0.2 A g^{-1} for the samples synthesized at different temperatures.

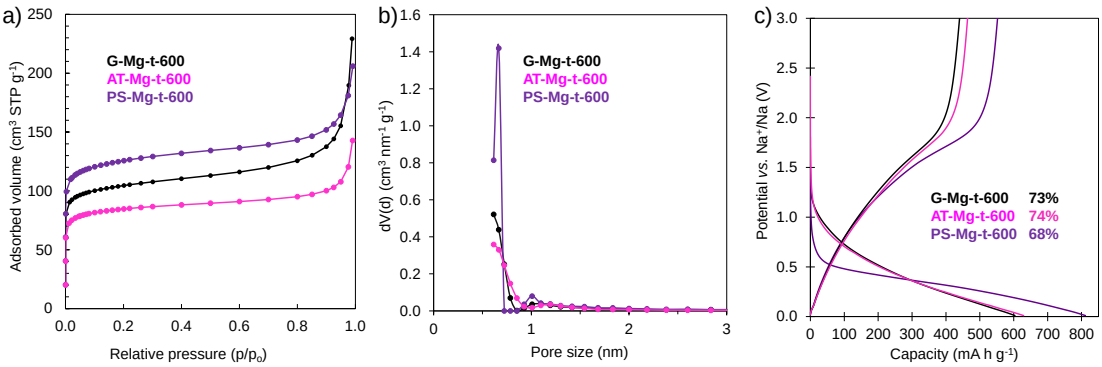

Figure S14. a) N_2 adsorption isotherms, b) pore size distributions and c) GCD profiles obtained at a current density of 0.1 A g^{-1} from 0.01 to 3 V *vs*. Na^+/Na (inset: ICE values) of the materials with different precursors.

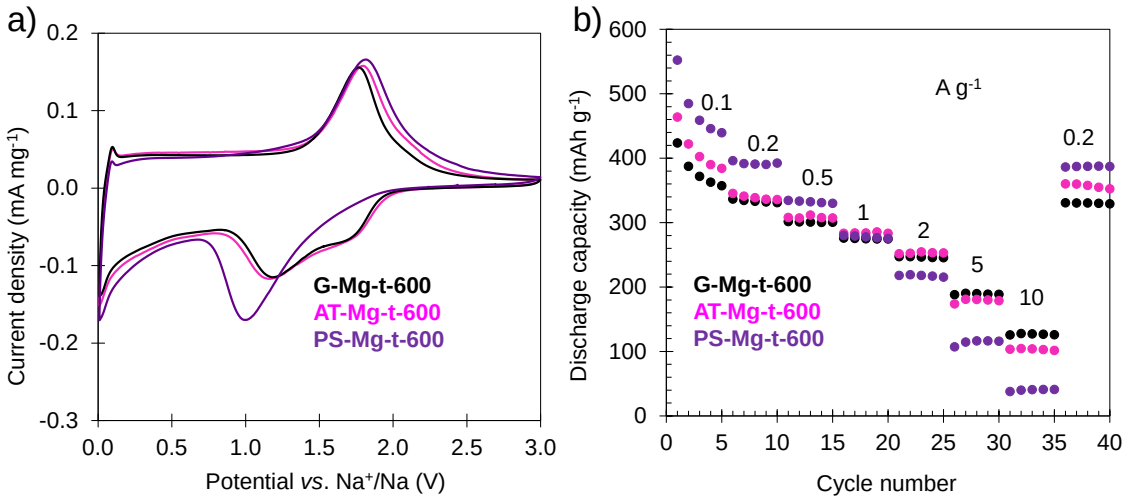

Figure S15. a) CVs plots recorded at a potential sweep rate of 0.1 mV s^{-1} from 0.01 to 3 V *vs*. Na^+/Na and b) impact of the current density on the reversible sodium storage capacity from 0.01 to 3 V *vs*. Na^+/Na for the materials obtained from different precursors.

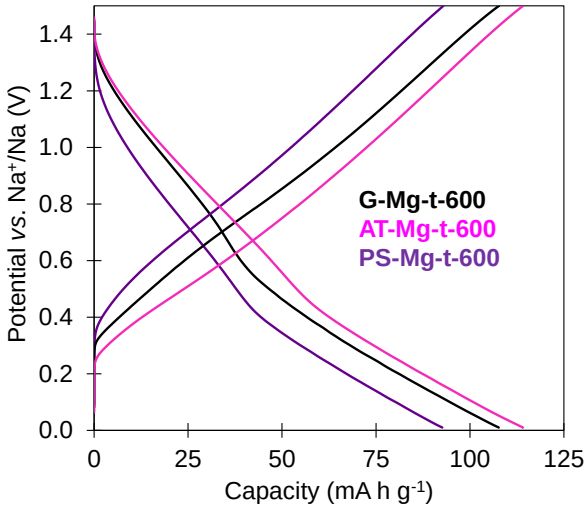

Figure S16. GCD profiles from 0.01 to 1.5 V *vs*. Na^+/Na obtained at a current density of 2 A g^{-1}.

Table S1. Sulfur content and values of specific capacity for S-doped carbon materials used as the negative electrode in sodium-ion batteries or sodium-ion capacitors using ester-based electrolytes.

Material	Doping agent	Doping agent/precursor ratio*	S content (wt%)	Carbon mass loading (mg cm^{-2})	Capacity at 0.1 A g^{-1} (mAh g^{-1})	Capacity at 5 A g^{-1} (mAh g^{-1})	Ref.
G-Mg-600	$MgSO_4$	1	26.2	~1	640	234	This work
G-Mg-t-600	$MgSO_4$ (NaCl)	1 (1.5)	16.1	~1	424	189	This work
S-HC-p[a]	S_8 (LiCl/KCl)	1 (10)[b]	13.66	n.a.	340	145	22
D-PHC-p[a]	$Na_2S_2O_3$ (LiCl/KCl)	2 (10)	14.07	n.a.	≈285	≈30	22
PNC	$Na_2S_2O_3$	2 (10)	13.21	0.7	631	≈50	23
SC-BDSA	K_2SO_4	8	40.1	3	≈580	n.d.	24
DC-S	S_8	1	26. 9	1-1.2	333	n.d.	25
S-CNS	S_8	2	≈23	~1	545	220	26
AGS-650[c]	S_8	3	12.8	~1	524	226	27
CS-600m[a]	S_8	3	26.7	1-1.2	550	264	28
SCNP-500	S_8	6	25.7	~1	726	186	29

***** The solvent/reactants weight ratio is given in parenthesis.
[a] The precursor was pre-carbonized at 400 ºC.
[b] Additional S was placed upstream in the furnace.
[c] The precursor was pre-carbonized at 550 ºC.

References

(1) VandeVondele, J.; Hutter, J. Gaussian Basis Sets for Accurate Calculations on Molecular Systems in Gas and Condensed Phases. *J. Chem. Phys.* **2007**, *127* (11), 114105.

(2) Goedecker, S.; Teter, M.; Hutter, J. Separable Dual-Space Gaussian Pseudopotentials. *Phys. Rev. B* **1996**, *54* (3), 1703–1710.

(3) Hartwigsen, C.; Goedecker, S.; Hutter, J. Relativistic Separable Dual-Space Gaussian Pseudopotentials from H to Rn. *Phys. Rev. B* **1998**, *58* (7), 3641–3662.

(4) Krack, M. Pseudopotentials for H to Kr Optimized for Gradient-Corrected Exchange-Correlation Functionals. *Theor. Chem. Acc.* **2005**, *114* (1–3), 145–152.

(5) Guidon, M.; Hutter, J.; Vandevondele, J. Auxiliary Density Matrix Methods for Hartree-Fock Exchange Calculations. *J. Chem. Theory Comput.* **2010**, *6* (8), 2348–2364.

(6) Hutter, J.; Iannuzzi, M.; Schiffmann, F.; Vandevondele, J. Cp2k: Atomistic Simulations of Condensed Matter Systems. *Wiley Interdiscip. Rev. Comput. Mol. Sci.* **2014**, *4* (1), 15–25.

(7) Kühne, T. D.; Iannuzzi, M.; Del Ben, M.; Rybkin, V. V.; Seewald, P.; Stein, F.; Laino, T.; Khaliullin, R. Z.; Schütt, O.; Schiffmann, F.; Golze, D.; Wilhelm, J.; Chulkov, S.; Bani-Hashemian, M. H.; Weber, V.; Borštnik, U.; Taillefumier, M.; Jakobovits, A. S.; Lazzaro, A.; Pabst, H.; Müller, T.; Schade, R.; Guidon, M.;

Andermatt, S.; Holmberg, N.; Schenter, G. K.; Hehn, A.; Bussy, A.; Belleflamme, F.; Tabacchi, G.; Glöß, A.; Lass, M.; Bethune, I.; Mundy, C. J.; Plessl, C.; Watkins, M.; VandeVondele, J.; Krack, M.; Hutter, J. CP2K: An Electronic Structure and Molecular Dynamics Software Package -Quickstep: Efficient and Accurate Electronic Structure Calculations. *J. Chem. Phys.* **2020**, *152* (19).

(8) Perdew, J. P.; Burke, K.; Ernzerhof, M. Generalized Gradient Approximation Made Simple [Phys. Rev. Lett. 77, 3865 (1996)]. *Phys. Rev. Lett.* **1997**, *78* (7), 1396.

(9) Johnson, E. R.; Becke, A. D. A Post-Hartree-Fock Model of Intermolecular Interactions: Inclusion of Higher-Order Corrections. *J. Chem. Phys.* **2006**, *124* (17), 174104.

(10) Becke, A. D.; Johnson, E. R. A Density-Functional Model of the Dispersion Interaction. *J. Chem. Phys.* **2005**, *123* (15), 154101.

(11) Allouche, A. Software News and Updates Gabedit — A Graphical User Interface for Computational Chemistry Softwares. *J. Comput. Chem.* **2012**, *32* (Sfb 858), 174–182.

(12) Grimme, S.; Antony, J.; Ehrlich, S.; Krieg, H. A Consistent and Accurate Ab Initio Parametrization of Density Functional Dispersion Correction (DFT-D) for the 94 Elements H-Pu. *J. Chem. Phys.* **2010**, *132* (15), 154104.

(13) Grimme, S.; Antony, J.; Schwabe, T.; Mück-Lichtenfeld, C. Density Functional Theory with Dispersion Corrections for Supramolecular Structures, Aggregates, and Complexes of (Bio)Organic Molecules. *Org. Biomol. Chem.* **2007**, *5* (5), 741–758.

(14) Olsson, E.; Cottom, J.; Cai, Q. Defects in Hard Carbon: Where Are They Located and How Does the Location Affect Alkaline Metal Storage? *Small* **2021**, *17* (18), 1–16.

(15) Olsson, E.; Chai, G.; Dove, M.; Cai, Q. Adsorption and Migration of Alkali Metals (Li, Na, and K) on Pristine and Defective Graphene Surfaces. *Nanoscale* **2019**, *11* (12), 5274–5284.

(16) Olsson, E.; Hussain, T.; Karton, A.; Cai, Q. The Adsorption and Migration Behavior of Divalent Metals (Mg, Ca, and Zn) on Pristine and Defective Graphene. *Carbon* **2020**, *163*, 276–287.

(17) Olsson, E.; Yu, J.; Zhang, H.; Cheng, H. M.; Cai, Q. Atomic-Scale Design of Anode Materials for Alkali Metal (Li/Na/K)-Ion Batteries: Progress and Perspectives. *Adv. Energy Mater.* **2022**, *12* (25).

(18) Olsson, E.; Cottom, J.; Au, H.; Titirici, M. M.; Cai, Q. Investigating the Effect of Edge and Basal Plane Surface Functionalisation of Carbonaceous Anodes for Alkali Metal (Li/Na/K) Ion Batteries. *Carbon* **2021**, *177*, 226–243.

(19) Olsson, E.; Cottom, J.; Alptekin, H.; Au, H.; Crespo-Ribadeneyra, M.; Titirici, M. M.; Cai, Q. Investigating the Role of Surface Roughness and Defects on EC Breakdown, as a Precursor to SEI Formation in Hard Carbon Sodium-Ion Battery Anodes. *Small* **2022**, *18* (43).

(20) Olsson, E.; Cottom, J.; Au, H.; Guo, Z.; Jensen, A. C. S.; Alptekin, H.; Drew, A.

J.; Titirici, M. M.; Cai, Q. Elucidating the Effect of Planar Graphitic Layers and Cylindrical Pores on the Storage and Diffusion of Li, Na, and K in Carbon Materials. *Adv. Funct. Mater.* **2020**, *30* (17).

(21) Alptekin, H.; Au, H.; Olsson, E.; Cottom, J.; Jensen, A. C. S.; Headen, T. F.; Cai, Q.; Drew, A. J.; Crespo Ribadeneyra, M.; Titirici, M. M. Elucidation of the Solid Electrolyte Interphase Formation Mechanism in Micro-Mesoporous Hard-Carbon Anodes. *Adv. Mater. Interfaces* **2022**, *9* (8), 1–12.

(22) Hong, Z.; Zhen, Y.; Ruan, Y.; Kang, M.; Zhou, K.; Zhang, J. M.; Huang, Z.; Wei, M. Rational Design and General Synthesis of S-Doped Hard Carbon with Tunable Doping Sites toward Excellent Na-Ion Storage Performance. *Adv. Mater.* **2018**, *30* (29), 1–9.

(23) Zhen, Y.; Sa, R.; Zhou, K.; Ding, L.; Chen, Y.; Mathur, S.; Hong, Z. Breaking the Limitation of Sodium-Ion Storage for Nanostructured Carbon Anode by Engineering Desolvation Barrier with Neat Electrolytes. *Nano Energy* **2020**, *74*, 104895.

(24) Wu, T.; Jing, M.; Yang, L.; Zou, G.; Hou, H.; Zhang, Y.; Zhang, Y.; Cao, X.; Ji, X. Controllable Chain-Length for Covalent Sulfur–Carbon Materials Enabling Stable and High-Capacity Sodium Storage. *Adv. Energy Mater.* **2019**, *9* (9), 1–11.

(25) Li, W.; Zhou, M.; Li, H.; Wang, K.; Cheng, S.; Jiang, K. A High Performance Sulfur-Doped Disordered Carbon Anode for Sodium Ion Batteries. *Energy Environ. Sci.* **2015**, *8* (10), 2916–2921.

(26) Zhao, G.; Yu, D.; Zhang, H.; Sun, F.; Li, J.; Zhu, L.; Sun, L.; Yu, M.; Besenbacher, F.; Sun, Y. Sulphur-Doped Carbon Nanosheets Derived from Biomass as High-Performance Anode Materials for Sodium-Ion Batteries. *Nano Energy* **2020**, *67* (July 2019), 104219.

(27) Payá, S.; Díez, N.; Sevilla, M. Biomass-Derived Carbon Sponges for Use as Sodium-Ion Capacitor Electrodes. *Sustain. Energy Fuels* **2023**, 2378–2389.

(28) Casal, M. D.; Díez, N.; Payá, S.; Sevilla, M. Cork-Derived Carbon Sheets for High-Performance Na-Ion Capacitors. *ACS Appl. Energy Mater.* **2023**, *6* (15), 8120–8131.

(29) Diez, N.; Sevilla, M.; Fuertes, A. B. A Dual Carbon Na-Ion Capacitor Based on Polypyrrole-Derived Carbon Nanoparticles. *Carbon* **2023**, *201*, 1126–1136.